Physica Scripta

INCLUSIVE PUBLISHING TRUSTED SCIENCE

PURPOSE-LED PUBLISHING™

PAPER • **OPEN ACCESS**

Load-dependent nanoindentation response of $NaBi(MoO_4)_2$ single crystals: PSR analysis and energy dissipation

To cite this article: M Isik *et al* 2026 *Phys. Scr.* **101** 335913

View the article online for updates and enhancements.

You may also like

- GUP-modified thermionic emission from individual carbon nanotubes
M Mohammadi Sabet and R Gholami
- Numerical simulation of the spatiotemporal evolution of linear disturbances in a semi-infinite fluid layer subjected to time-periodic temperature and heat-flux forcings
Mohamed Sakine, Mehdi Riahi, Mohamed Hayani Choujaa et al.
- Chaos game optimization framework to engineer custom microwave absorbers for RCS reduction
Ranjeet Pratap Singh Bhadoriya and Ravi Panwar

This content was downloaded from IP address 194.27.6.19 on 31/08/2026 at 22:59

Physica Scripta

Check for updates

OPEN ACCESS

RECEIVED
10 April 2026

REVISED
5 June 2026

ACCEPTED FOR PUBLICATION
10 August 2026

PUBLISHED
18 August 2026

Original content from this work may be used under the terms of the Creative Commons Attribution 4.0 licence.

Any further distribution of this work must maintain attribution to the author(s) and the title of the work, journal citation and DOI.

PAPER

Load-dependent nanoindentation response of $NaBi(MoO_4)_2$ single crystals: PSR analysis and energy dissipation

M Isik[1,*], **G Altuntas**[2] and **N M Gasanly**[3,4]

[1] Department of Biomedical Engineering, Faculty of Engineering and Architecture, Izmir Bakircay University, 35665 Izmir, Türkiye
[2] Faculty of Technology, Department of Metallurgical and Materials Engineering, Gazi University, Ankara, Türkiye
[3] Department of Physics, Middle East Technical University, Ankara 06800, Türkiye
[4] Virtual International Scientific Research Centre, Baku State University, Baku 1148, Azerbaijan
[*] Author to whom any correspondence should be addressed.

E-mail: mehmet.isik@bakircay.edu.tr

Keywords: $NaBi(MoO_4)_2$ single crystal, nanoindentation, indentation size effect, proportional specimen resistance model, Young's modulus, energy dissipation

Abstract

In the present study, $NaBi(MoO_4)_2$ single crystals grown by the Czochralski method were systematically investigated through structural characterization and depth-sensing nanoindentation. X-ray diffraction confirmed phase purity and tetragonal symmetry, while Williamson–Hall analysis provided complementary insight into crystallite-scale strain and defect-related broadening. Load-dependent nanoindentation measurements were evaluated using Oliver–Pharr analysis together with proportional specimen resistance and Meyer-based approaches to distinguish apparent indentation effects from intrinsic mechanical behavior. The results reveal a clear indentation size effect, a progressive decrease in apparent hardness/modulus-related indicators with increasing load, and a concurrent shift in energy partition from elastic to plastic contribution, consistent with increasing irreversible deformation at higher contact loads. By combining crystallographic, mechanical, and energetic analyses within a single framework, this work delivers a reliable property map for $NaBi(MoO_4)_2$ and provides practical guidance for its use in load-sensitive photonic, optoelectronic, and functional oxide applications where mechanical reliability is critical.

1. Introduction

$NaBi(MoO_4)_2$ belongs to the family of complex molybdate crystals that have attracted sustained attention because of their multifunctional physical behavior, structural flexibility, and chemical stability under technologically relevant conditions. As a bismuth-containing double molybdate, this compound combines the stereochemical activity of Bi^{3+} with the robust tetrahedral framework associated with molybdate units, giving rise to a rich set of optical, dielectric, and thermal characteristics [1–3]. Such a combination makes $NaBi(MoO_4)_2$ a promising candidate for advanced functional materials design, especially in fields where performance depends on coupled responses rather than a single property. In practical terms, molybdate-based oxides are widely explored for photonic components, phosphor hosts, luminescent centers, photocatalytic systems, and sensing platforms, and $NaBi(MoO_4)_2$ is increasingly considered within this broader context [4–7]. The compound is also notable from a crystal-chemistry perspective, since cation ordering, local coordination environment, and defect population can be tuned during synthesis, thereby enabling tailored behavior for specific engineering targets. These features position $NaBi(MoO_4)_2$ not merely as an interesting oxide, but as a potentially useful material for next-generation optoelectronic devices, energy-related components, and multifunctional ceramic architectures where structural durability and functional reliability must coexist [8–10].

Beyond this general framework, previous studies on $NaBi(MoO_4)_2$ and related bismuth molybdates have emphasized performance-relevant phenomena such as optical absorption behavior [11], band-gap-sensitive responses, photoluminescence characteristics [12], and thermally stable structural phases [13].

© 2026 The Author(s). Published by IOP Publishing Ltd

In several application-driven investigations, researchers have focused on how compositional control, sintering parameters, and crystal quality influence electronic polarization, defect-assisted transitions, and light–matter interaction mechanisms. These efforts are particularly relevant for applications in phosphor-converted systems, optical conversion media, dielectric elements, and catalytic environments where stability and repeatability are essential [14–16]. In addition, comparative work across scheelite-like and related molybdate structures has shown that subtle changes in cation distribution can strongly affect local bonding rigidity, anisotropic response, and microstructural evolution, all of which are critical for real-device performance. $NaBi(MoO_4)_2$, in this sense, represents a useful model material that bridges functional behavior and structural complexity. Its potential utility in photonic and electronic material stacks depends not only on intrinsic optical or electrical attributes but also on process compatibility, polishing quality, and tolerance to contact-induced stress during fabrication and service. Therefore, while the literature has provided valuable insights into physicochemical and application-oriented aspects of this compound, an important dimension remains underexplored: the direct, quantitative assessment of its small-scale mechanical response under controlled loading.

Determining the mechanical properties of $NaBi(MoO_4)_2$ is crucial for moving from material-level promise to device-level implementation. Functional crystals are routinely exposed to local stresses during cutting, grinding, polishing, thin-film integration, wire bonding, packaging, and long-term operation; consequently, insufficient knowledge of hardness, elastic modulus, and deformation resistance can become a bottleneck for manufacturability and reliability [17–19]. Nanoindentation offers a powerful and highly localized route to resolve these issues because it provides simultaneous load–displacement data, enables extraction of hardness and Young's modulus at micrometer-to-nanometer length scales, and reveals load-dependent phenomena such as the indentation size effect (ISE). For brittle or quasi-brittle crystalline oxides, such measurements are especially informative, as they help identify the transition between elastic-dominant and damage-prone regimes and support the optimization of processing windows [20]. In this study, we present a systematic nanoindentation investigation of $NaBi(MoO_4)_2$ crystal under different applied loads and evaluate its mechanical response in terms of hardness and Young's modulus while analyzing the observed ISE behavior. To the best of our knowledge, nanoindentation measurements on $NaBi(MoO_4)_2$ have not been reported previously. This first-time experimental assessment constitutes the central originality of our work and provides a foundational mechanical dataset for future design, modeling, and application-oriented development of $NaBi(MoO_4)_2$-based functional components. Beyond the first experimental reporting of nanoindentation data, the scientific contribution of the present work lies in linking the load-dependent mechanical response of $NaBi(MoO_4)_2$ to its crystal-chemical characteristics. In this compound, the mechanically active framework is governed by relatively rigid MoO_4 tetrahedral units, charge-balancing Na^+ sites, and Bi^{3+} cations with stereochemically active lone-pair electrons. Such local structural features can promote anisotropic bonding, lattice distortion, and defect-assisted deformation under concentrated contact loading. Therefore, the ISE, the reduction in apparent modulus with increasing load, and the change in elastic/plastic work partition are discussed not merely as empirical trends, but as manifestations of the interaction between contact-induced deformation and the crystal chemistry of the bismuth molybdate framework.

2. Experimental details

$NaBi(MoO_4)_2$ single crystals were grown by the Czochralski method using high-purity precursor powders of Bi_2O_3 (99.9%), MoO_3 (99.5%), and Na_2CO_3 (99.5%) obtained from Sigma-Aldrich. The starting composition was prepared in the stoichiometric ratio $1Bi_2O_3$:$4MoO_3$:$1Na_2CO_3$. First, the precursor powders were thoroughly ground and homogenized, and the mixed batch was then pressed into pellet form to improve reaction uniformity. To obtain a single-phase feed material, the pellets were calcined at 800 °C for 20–24 h. Crystal growth was subsequently carried out under a pulling rate of 2 mm h^{-1} and a rotation speed of 15 rpm. After completion of the growth process, the boule was cooled to room temperature at a controlled cooling rate of 30 K h^{-1} to minimize thermal stress and crack formation. Finally, the as-grown bulk crystal was carefully cut into smaller specimens with approximate dimensions of $15 \times 12 \times 1$ mm^3 for subsequent structural and nanoindentation measurements.

Nanoindentation measurements were performed on the mechanically polished broad surface of the cut single-crystal specimen. Previous single-crystal XRD measurements performed by our research group on the $NaBi(MoO_4)_2$ crystal used in the present study showed dominant (004) and (008) reflections, indicating that the broad crystal surface is preferentially oriented along the (00*l*) family of planes [14]. Based on this crystallographic evidence, the indented surface in the present study was considered to

be nominally (00*l*)-oriented. However, since no additional Laue back-reflection, EBSD, or orientation-resolved XRD measurement was performed on the exact indented specimen, the reported hardness and Young's modulus values should be interpreted as effective indentation properties of the tested surface rather than as a complete orientation-dependent mechanical dataset. Nanoindentation measurements were carried out using a CSM Instruments nanoindentation platform equipped with a standard diamond Berkovich indenter tip. Prior to the nanoindentation measurements, the instrument was calibrated by the technical specialist of the research center using a fused silica reference specimen, following the general recommendations of ISO 14 577 for instrumented indentation testing. The calibration included verification of the load–displacement response, frame compliance correction, and indenter area-function calibration for the Berkovich tip. The obtained calibration parameters were then applied to all $NaBi(MoO_4)_2$ indentation data during the Oliver–Pharr analysis. An approach velocity of 2000 nm min^{-1} was selected to achieve stable contact while reducing near-surface artifacts associated with excessively slow engagement. Indentation experiments were performed at multiple peak loads between 5 and 250 mN. At each load level, 8–10 indents were performed at different positions on the sample surface to improve statistical reliability and reduce local surface-related bias. Outlier rejection was carried out using both curve-shape inspection and statistical consistency criteria. Indents were excluded only when the load–displacement curve exhibited clear experimental artifacts, such as unstable initial contact, abnormal discontinuities, surface-defect-related response, or when the calculated hardness/contact-depth value deviated by more than approximately two standard deviations from the mean value obtained at the same load. Depending on the load level, approximately 0–2 indents were excluded, and at least 7–9 valid indents were retained for the final mechanical analysis. For each loading condition, both loading and unloading segments were controlled at a rate equal to $2F_{max}$ per minute, which corresponds to an approximately constant loading time of 30 s to reach the selected maximum load. A short 1 s hold was applied at maximum load before unloading as a brief instrumental stabilization step. However, this hold period was not intended to suppress, fully capture, or quantitatively evaluate transient creep deformation. Because the absolute loading/unloading rates and indentation depths vary with the selected maximum load, possible rate-dependent and creep-related contributions cannot be completely excluded. Therefore, the nanoindentation-derived hardness, Young's modulus, proportional specimen resistance (PSR) parameters, and energy terms reported in this work should be interpreted as apparent/effective indentation parameters obtained under the present testing protocol, rather than as fully creep-independent intrinsic material constants.

3. Results and discussion

3.1. XRD analysis

Figure 1 presents the XRD pattern of the $NaBi(MoO_4)_2$ crystal. For XRD analysis, a small portion of the grown crystal was gently ground into powder in order to reduce the effect of single-crystal orientation and to obtain a diffraction pattern more representative of the bulk phase. In powder XRD measurements, the crystallites are randomly oriented, and the observed reflections arise from crystallographic planes that satisfy the Bragg diffraction condition within the selected measurement geometry and 2θ range. Therefore, the observation of nine distinct diffraction peaks is mainly associated with the dominant diffracting planes of tetragonal $NaBi(MoO_4)_2$ and the reflections that could be clearly resolved above the background under the present measurement conditions. A total of nine distinct diffraction peaks were observed in the measured 2θ range, indicating good crystallinity and phase formation. The peak positions are consistent with a tetragonal crystal structure, confirming that the synthesized crystal preserves the expected symmetry. No additional strong reflections attributable to secondary impurity phases were detected within the sensitivity of the measurement, which supports the phase purity of the grown sample and agrees with the crystal-growth conditions. For quantitative structural evaluation, lattice parameters were estimated from selected reflections. Using the (200) peak observed at $2\theta = 34.13°$, the lattice parameter a was calculated as 5.25 Å. In addition, from the (112) reflection observed at $2\theta = 28.68°$, the lattice parameter c was determined as 11.39 Å. These values are internally consistent with a tetragonal $NaBi(MoO_4)_2$ framework and provide a reliable structural basis for interpreting the subsequent mechanical measurements [12]. In particular, confirming the tetragonal phase and extracting realistic lattice constants are important because nanoindentation response is strongly linked to crystallographic arrangement, bond anisotropy, and defect distribution. Therefore, XRD results not only verify successful crystal growth but also establish that the hardness and elastic modulus values discussed in the following sections are representative of the intended $NaBi(MoO_4)_2$ phase.

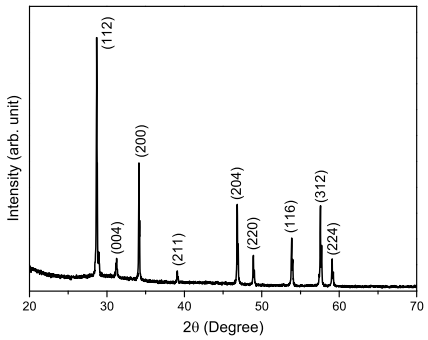


Figure 1. XRD pattern of $NaBi(MoO_4)_2$ crystal showing the indexed peaks consistent with tetragonal symmetry.

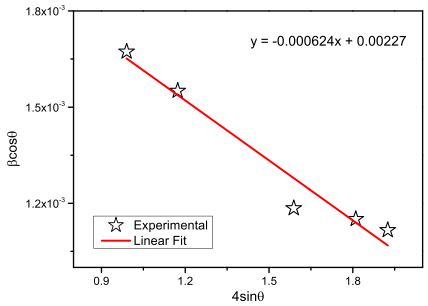


Figure 2. Williamson–Hall plot obtained from the XRD peak broadening analysis of $NaBi(MoO_4)_2$. The linear fit was used to estimate microstrain and crystallite size.

To further quantify the microstructural state of the $NaBi(MoO_4)_2$ crystal, the XRD peak broadening was analyzed using the Williamson–Hall (W–H) method, as shown in figure 2. In this approach, the total integral broadening is considered as a combined contribution of finite crystallite size and lattice strain. Before applying the W–H analysis, the measured peak broadening was corrected for instrumental broadening. The instrumental contribution was estimated from a standard reference measurement recorded under the same XRD configuration. The corrected broadening value, β, was then obtained using

$$\beta = \left(\beta_{\text{meas}}^2 - \beta_{\text{inst}}^2\right)^{1/2}, \tag{1}$$

where β_{meas} is the measured full width at half maximum (FWHM, in radians) of the $NaBi(MoO_4)_2$ diffraction peak and β_{inst} is the instrumental FWHM contribution. All FWHM values were converted from degrees to radians before being used in the W–H plot. The linearized W–H relation is written as [21]

$$\beta\cos\theta = \frac{k\lambda}{D} + 4\varepsilon\sin\theta, \tag{2}$$

where θ is the Bragg angle, k is the Scherrer constant (taken as 0.94), λ is the x-ray wavelength, D is the crystallite size, and ε is the microstrain. By fitting the $\beta\cos\theta$ versus $4\sin\theta$ data, the slope gives ε and the intercept gives $k\lambda/D$. The linear regression of the W–H plot yielded a negative slope, corresponding to a microstrain value of $\varepsilon = (-6.24 \pm 0.78) \times 10^{-4}$. This sign indicates that the dominant residual lattice distortion is compressive rather than tensile; in other words, the diffraction-line broadening includes a compressive strain contribution in the analyzed crystallographic directions [22, 23]. At the same time, the small absolute magnitude still points to a relatively low overall strain level in the grown crystal. The crystallite size extracted from the intercept was approximately $D \approx 64 \pm 3$ nm. It should be emphasized that this value corresponds to the coherent diffraction domain size derived from XRD peak broadening and does not represent the actual grain size or macroscopic size of the grown bulk single crystal. Therefore, in the present single-crystal specimen, $D \approx 64$ nm should be interpreted only as the average size of coherently diffracting domains within the crystal.

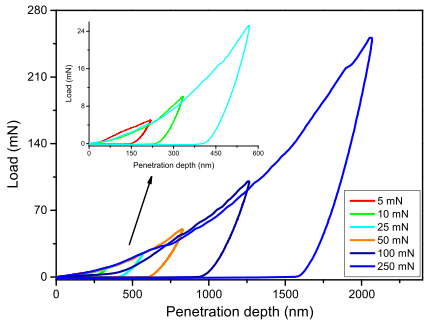


Figure 3. Load–displacement nanoindentation curves of $NaBi(MoO_4)_2$ crystal obtained at different peak loads.

$$\delta = \frac{1}{D^2}. \tag{3}$$

Using $D \approx 64$ nm, the dislocation density is on the order of $\delta \approx 2.4 \times 10^{14}\ \mathrm{m}^{-2}$. Together, these W–H results confirm that the $NaBi(MoO_4)_2$ crystal possesses low microstrain and moderate defect density, which are favorable for reliable interpretation of the subsequent nanoindentation-derived mechanical parameters.

3.2. Nanoindentation analysis

The nanoindentation response of $NaBi(MoO_4)_2$ was further evaluated under different peak loads. An additional methodological point should be considered when interpreting the load-dependent indentation response. In the present protocol, the loading rate was scaled with the maximum load as $2F_{max}$ per minute; therefore, the time required to reach the peak load was kept approximately constant at 30 s for all load levels. This choice provides a consistent normalized loading history. Nevertheless, the absolute loading and unloading rates differ by more than one order of magnitude between the lowest and highest loads, and the corresponding penetration depths and deformation volumes are also different. As a result, the load–displacement curves obtained at different maximum loads should not be interpreted as being fully equivalent in terms of creep or rate-dependent deformation state. The 1 s hold at maximum load is too short to establish a creep-equilibrated condition. Consequently, the observed load dependence of hardness, Young's modulus, PSR-derived parameters, and indentation work components may include not only ISE and deformation-volume effects, but also possible contributions from rate-dependent and transient creep deformation. For this reason, the following discussion emphasizes apparent/effective load-dependent indentation behavior under the present experimental protocol, rather than claiming fully rate-independent intrinsic mechanical properties. The corresponding load–displacement behavior presented in figure 3 clearly show the expected increase in penetration depth with increasing load and provide the basis for extracting reliable mechanical parameters. The absence of severe discontinuities in the loading segments suggests that the tests were performed in a stable contact regime. At the same time, the load dependence of the indentation response indicates the presence of an ISE, which is consistent with the behavior already discussed for this crystal system [24, 25]. Although the nanoindentation-derived parameters are presented as a function of applied peak load, the applied load directly determines the corresponding penetration/contact depth and deformation volume, as shown by the load–displacement curves in figure 3. Therefore, the load-dependent trends discussed in all presented figures within the manuscript can also be interpreted as reflecting the depth-dependent evolution of the sampled deformation volume. In the present study, the load-based representation was retained because it is widely used in ISE, PSR, and Meyer-law analyses and allows direct comparison with the applied testing conditions. It should also be noted that the penetration/contact depths reached during the nanoindentation measurements are larger than the W–H coherence length of approximately 64 nm. Thus, the measured mechanical response represents an effective near-surface response averaged over a deformation volume larger than the XRD-derived coherent domain size, rather than the response of an individual coherently diffracting region. The possible influence of crystallographic anisotropy should also be considered. Since the indented surface is nominally associated with the (00*l*) orientation, the present nanoindentation results mainly reflect the mechanical response normal to this preferentially oriented broad surface. In tetragonal single crystals, differences in bonding configuration and elastic stiffness along different crystallographic directions may affect the measured indentation modulus and hardness. Therefore, future nanoindentation studies

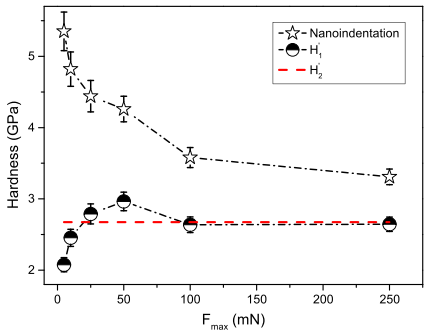


Figure 4. Load-dependent nanoindentation hardness results obtained by Oliver–Pharr analysis, together with PSR-based true and load-independent hardness values.

on deliberately indexed crystal planes would be useful for establishing the full anisotropic mechanical behavior of $NaBi(MoO_4)_2$. Mechanical parameters obtained from the Oliver–Pharr analysis are summarized as a function of load in figure 4. In addition to the directly calculated hardness values, the PSR-based load-independent parameters are also shown for comparison. The analysis was performed using the PSR relation [26, 27]

$$\frac{F_{\max}}{h_c} = \delta_1 + \delta_2 h_c, \tag{4}$$

where $F_{\max}$ is the maximum applied load and h_c is the contact depth. From the linear fit, the coefficients were determined as $\delta_1 = 0.0168\,\mathrm{mN\,nm^{-1}}$ and $\delta_2 = 6.55 \times 10^{-5}\,\mathrm{mN\,nm^{-2}}$.

In the Oliver–Pharr analysis, the contact area was calculated using the calibrated indenter area function obtained from the fused silica calibration. For the PSR treatment, the contact area was first expressed in a general form as $A_c(h_c)$. Accordingly, the true hardness value (H_1') can be written as [28]

$$H_1' = \frac{F_{\max} - \delta_1 h_c}{A_c\,(h_c)}. \tag{5}$$

For an ideal Berkovich geometry, $A_c(h_c) = 24.5h_c^2$, which gives

$$H_1' = \frac{F_{\max} - \delta_1 h_c}{24.5 h_c^2}. \tag{6}$$

Similarly, the load-independent hardness parameter is obtained as

$$H_2' = \frac{\delta_2}{24.5}. \tag{7}$$

Thus, the directly reported Oliver–Pharr hardness values were obtained using the calibrated area function, whereas the PSR-derived parameters were used as comparative load-independent indicators based on the ideal Berkovich area approximation. The agreement between the PSR-corrected trend and the experimental hardness evolution confirms that a significant part of the load dependence arises from near-surface and geometrically induced effects rather than from a true intrinsic variation of hardness.

To further support the ISE interpretation, the Meyer law analysis was also applied, as shown in figure 5. In this framework, the indentation load follows $F_{\max} = Ah^n$, where n is the Meyer index [29, 30]. The fitted exponent was found to be $n = 1.72$. Since $n < 2$, the result indicates normal ISE behavior, meaning that the apparent hardness decreases with increasing load. This observation is fully consistent with both the Oliver–Pharr and PSR-based evaluations. Overall, the combined analysis demonstrates that $NaBi(MoO_4)_2$ exhibits a clear load-dependent indentation response at low-to-intermediate loads, while the PSR-corrected parameters provide a more representative estimate of intrinsic hardness for material-level comparison. From a mechanistic point of view, the normal ISE observed in $NaBi(MoO_4)_2$ can be associated with the progressive activation of a larger deformation volume beneath the Berkovich indenter. At shallow penetration depths, the response is dominated by near-surface constraint, geometrically necessary defects, and the resistance of the relatively rigid MoO_4 tetrahedral framework. As the load increases, the deformation zone extends into a larger volume where local lattice distortion, pre-existing defect populations, and the stereochemical activity of Bi^{3+} lone-pair electrons may facilitate irreversible

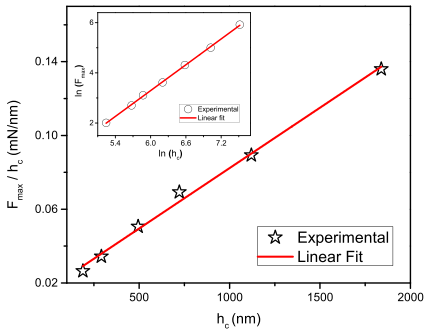


Figure 5. PSR and Meyer-law-based linear analysis used to extract δ_1, δ_2, and the Meyer exponent n for $NaBi(MoO_4)_2$ nanoindentation data.

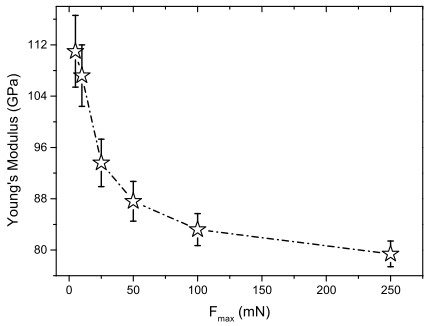


Figure 6. Variation of Young's modulus with applied indentation load for $NaBi(MoO_4)_2$, obtained from Oliver–Pharr analysis.

deformation and contact-induced compliance. Thus, the decrease in apparent hardness with increasing load is not interpreted only as a mathematical ISE trend, but also as a crystal-chemistry-dependent response of the Na–Bi–Mo–O framework to localized mechanical loading.

The load dependence of Young's modulus is shown in figure 6. The Oliver–Pharr-derived modulus values exhibit a decreasing trend with increasing indentation load, which is consistent with the behavior expected for brittle crystals in the presence of indentation-induced damage. Quantitatively, the Young's modulus decreases from 111.0 GPa at 5 mN to 79.4 GPa at 250 mN. Overall, this corresponds to a total reduction of approximately 28.5% between the minimum and maximum applied loads. This reduction should be regarded as an apparent contact modulus decrease rather than a change in the intrinsic elastic constant of the crystal. In complex molybdate oxides, the elastic response is expected to be influenced by the connectivity of MoO_4 tetrahedra, the local coordination environment of Bi^{3+}, and defect-assisted lattice distortion. With increasing indentation depth, the measured stiffness increasingly reflects an averaged response over a larger deformation volume, where local structural disorder, non-uniform strain fields, and irreversible deformation can reduce the effective unloading stiffness. At relatively low loads, the measured response is more strongly influenced by near-surface effects and the ISE, whereas at higher loads the larger deformation volume may promote local damage accumulation and contact-induced compliance, leading to an apparent reduction in elastic modulus. Since the individual load–displacement curves do not show clear pop-in events, abrupt discontinuities, or distinct slope changes that can be unambiguously assigned to crack initiation, microcracking is not claimed here as a directly observed mechanism. Instead, the modulus reduction is interpreted more cautiously in terms of possible damage-assisted compliance and increasing irreversible deformation at larger indentation depths [31]. This trend is in line with previous nanoindentation studies on brittle ceramics and oxide crystals, where both hardness and modulus were reported to decrease as the applied load increased. To interpret this behavior, the load–Young's modulus curve can be extrapolated toward zero load to estimate the intrinsic (damage-minimized) modulus, E_i. In practical terms, the reduction in effective contact stiffness at higher loads may arise from a combination of larger deformation volume, defect-assisted irreversible deformation, and possible sub-surface damage, rather than from a purely intrinsic change in the elastic constant. Therefore, the experimentally observed load-dependent modulus should be evaluated together with crack-assisted compliance effects rather than being treated as a purely intrinsic elastic constant. Overall,

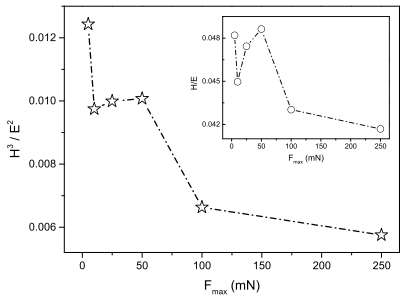


Figure 7. Variation of H^3/E^2 with applied load for $NaBi(MoO_4)_2$; inset shows the corresponding H/E–F_{max} relation.

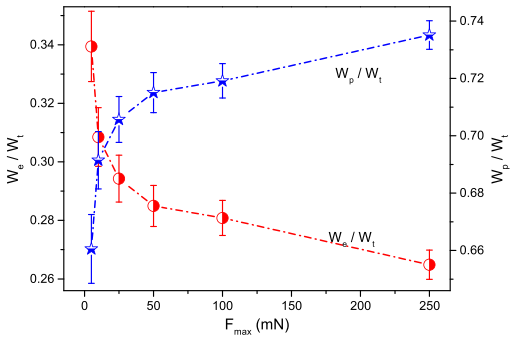


Figure 8. Variation of normalized elastic work (W_e/W_t) and plastic work (W_p/W_t) with applied indentation load for $NaBi(MoO_4)_2$.

the figure 6 results support the conclusion that $NaBi(MoO_4)_2$ shows stable elastic behavior at low-to-moderate loads, while progressive contact damage at higher loads contributes to the apparent decrease in Young's modulus.

In addition to the load dependence of hardness and Young's modulus, the combined resistance indicators H^3/E^2 and H/E were evaluated as a function of applied load (figure 7) [32]. The parameter H^3/E^2, which is commonly associated with resistance to plastic deformation, shows a clear decrease with increasing load, especially beyond 50–100 mN, indicating that the apparent resistance to localized permanent deformation becomes lower at higher loads. A similar trend is observed for the H/E ratio (inset), which gradually decreases toward high loads after a relatively higher level in the low-load regime. This behavior is consistent with the ISE-dominated response at low loads and crack-/damage-assisted softening effects at higher loads. Therefore, figure 7 supports the conclusion that the mechanical response of $NaBi(MoO_4)_2$ is load sensitive, and that intrinsic material comparisons should preferentially rely on corrected or load-independent parameters derived from the PSR/Oliver–Pharr framework.

Figure 8 shows the load dependence of the normalized elastic and plastic work components obtained from nanoindentation, expressed as W_e/W_t and W_p/W_t, where W_e is the elastic work (recoverable indentation energy), W_p is the plastic work (irreversible dissipation energy), and W_t is the total indentation work ($W_t = W_e + W_p$) [33]. A clear opposite trend is observed for the two ratios as the load increases. The elastic work fraction decreases from approximately 0.34 at low load to about 0.265 at 250 mN, while the plastic work fraction increases from about 0.66 to nearly 0.73 over the same load range. This complementary behavior indicates that the contribution of irreversible deformation becomes progressively more dominant at higher indentation loads. At low loads, the relatively higher W_e/W_t values imply that a larger portion of the input energy is stored and recoverable during unloading, consistent with stronger elastic recovery in the near-surface regime. With increasing load, however, the rise in W_p/W_t suggests enhanced dissipation through irreversible deformation mechanisms, such as defect accumulation, local structural disorder, and damage-assisted contact softening [34]. Figure 8 provides an additional energetic perspective confirming that $NaBi(MoO_4)_2$ exhibits a load-dependent transition from relatively elastic-dominant response at low loads to increasingly plastic/damage-dominant behavior at high loads.

It is also useful to place the present results in the broader context of molybdate- and tungstate-based oxide systems. In such materials, the mechanical response is generally governed by the balance between relatively rigid tetrahedral anionic groups, cation coordination polyhedra, and defect-mediated local distortion [35]. Compared with simple oxide ceramics, double molybdates such as $NaBi(MoO_4)_2$ possess a more complex cation sublattice, where the coexistence of Na^+ and Bi^{3+} can introduce local bonding heterogeneity [36]. In particular, the stereochemically active Bi^{3+} lone pair may contribute to asymmetric coordination and local lattice softness, whereas the MoO_4 tetrahedra provide comparatively rigid structural units [37]. The measured load-independent hardness of approximately 2.67 GPa and the decrease in apparent modulus with increasing load therefore suggest that $NaBi(MoO_4)_2$ behaves as a moderately hard but contact-sensitive functional oxide. This behavior is consistent with the general expectation for complex molybdate/tungstate crystals, in which mechanical stability is controlled not only by bond strength but also by cation disorder, local strain, and the ability of the lattice to accommodate indentation-induced deformation.

4. Conclusion

In this work, $NaBi(MoO_4)_2$ single crystals grown by the Czochralski method were structurally and mechanically characterized in detail. XRD results confirmed a tetragonal phase with nine identifiable peaks, and lattice parameters were determined as $a = 5.25$ Å and $c = 11.39$ Å. W–H analysis showed a negative slope corresponding to a compressive microstrain of $\varepsilon = -6.2 \times 10^{-4}$, while the dislocation density was estimated as $\sim 2.4 \times 10^{14}\ m^{-2}$. These findings indicate good crystallinity with moderate defect content and provide a reliable structural basis for interpreting the nanoindentation response. Nanoindentation analyses revealed a clear load-dependent mechanical behavior (ISE regime). The PSR/Meyer evaluations gave Meyer index as $n = 1.72$, confirming normal ISE. The measured hardness decreased from 5.35 GPa at 5 mN to 3.31 GPa at 250 mN, while the PSR-based load-independent hardness converged to about 2.67 GPa. Young's modulus decreased from 111.0 GPa at 5 mN to 79.4 GPa at 250 mN, corresponding to an approximately 28.5% reduction. Since no clear discontinuities or slope changes were observed in the load–displacement curves, this decrease is not attributed to directly evidenced microcrack initiation. Instead, it is interpreted as an apparent modulus reduction associated with increasing indentation depth, larger deformation volume, possible sub-surface damage, and enhanced irreversible deformation at higher loads. Overall, the combined structural, energetic, and indentation analyses show that $NaBi(MoO_4)_2$ exhibits stable behavior at low loads but progressively more irreversible deformation at higher loads; therefore, PSR-corrected/load-independent parameters are essential for reporting intrinsic mechanical properties of this crystal. These results confirm that $NaBi(MoO_4)_2$ is a promising candidate for photonic, optoelectronic, and functional oxide applications where load-sensitive mechanical reliability is a key design criterion.

Data availability statement

All data that support the findings of this study are included within the article (and any supplementary files).

Funding

This work was supported by the Scientific and Technological Research Council of Turkey (TUBITAK), Project No: 125F317.

Author contributions

M Isik 0000-0003-2119-8266
Formal analysis (lead), Investigation (lead), Methodology (supporting), Writing – original draft (lead)

G Altuntas 0000-0003-4504-0850
Formal analysis (supporting), Methodology (lead)

N M Gasanly 0000-0002-3199-6686
Resources (lead), Supervision (supporting), Writing – review & editing (supporting)

References

[1] Kshetrapal S, Ugemuge N S, Sharma K, Nafdey R and Moharil S 2025 Luminescence of some lanthanide activators in $NaBi(MoO_4)_2$ *J. Opt.* **54** 1430–38
[2] Krupych O, Kushnirevych M, Mys O and Vlokh R 2015 Photoelastic properties of $NaBi(MoO_4)_2$ crystals *Appl. Opt.* **54** 5016–23
[3] Khusravbekov L, Kholov A and Charnaya E V 2015 Acoustic investigation of $NaBi(MoO_4)_2$ and $NaBi(WO_4)_2$ crystals at high temperatures *Bull. Russ. Acad. Sci. Phys.* **79** 1306–09
[4] Xie J, Cheng L, Tang H, Yu X, Wang Z, Mi X, Liu Q and Zhang X 2022 Synthesis and photoluminescence properties of NUV-excited $NaBi(MoO_4)_2$: Sm^{3+} phosphors for white light emitting diodes *Opt. Laser Technol.* **147** 107659
[5] Liu L, Wang H, Zhang X and Lin Z 2016 Synthesis of novel $RuO_2/NaBi(MoO_4)_2$ nanosheets composite and its gas sensing performances towards ethanol *Sens. Actuators B* **237** 275–83
[6] Su W, Zhang M, Zhang C, Zou Y, Liu W and Ding S 2025 Upconversion luminescence and optical thermometry behaviors of Yb^{3+} and Ho^{3+} co-doped $NaBi(MoO_4)_2$ single crystal *J. Mol. Struct.* **1343** 142855
[7] Kunchala R K, Kalia R and Naidu B S 2020 Upconversion luminescence properties of $NaBi(MoO_4)_2$: ln^{3+}, Yb^{3+} ($Ln = Er^{3+}$, Ho^{3+}) nanomaterials synthesized at room temperature *Ceram. Int.* **46** 18614–22
[8] Zhu C, Du F, Fu P, Wang S and Lin Z 2018 Highly sensitive sensor based on $NaBi(MoO_4)_2$/MWCNT composites *Mater. Res. Express* **5** 125016
[9] Li Y, Cao T, Mei Z, Li X and Sun D 2020 Separating type I heterojunction of $NaBi(MoO_4)_2/Bi_2MoO_6$ by TiO_2 nanofibers for enhanced visible-photocatalysis *Chem. Phys.* **533** 110696
[10] Yang W, He X, He T, Li Y, Yang J, Huang H and Cui S 2024 Broad spectral response of Y-$NaBi(MoO_4)_2$@ $NaYF_4$: Yb^{3+}, Tm^{3+} photocatalysts for efficient degradation of ciprofloxacin: upconversion mechanism and theoretical calculations *Ceram. Int.* **50** 46904–15
[11] Pepe Y, Yildiz E A, Isik M, Karatay A, Gasanly N and Elmali A 2023 Tunable nonlinear absorption and optical limiting behavior of $NaBi(Mo_xW_1 - _xO_4)_2$ single crystals with ratio of Molybdenum/Tungsten *Phys. Scr.* **98** 075922
[12] Muskan, Sharma P, Deepali and Jayasimhadri M 2023 Exploration of efficient photoluminescence properties of intense green emitting Er^{3+} activated $NaBi(MoO_4)_2$ phosphor for white LED applications *J. Mater. Res.* **38** 4655–64
[13] Calderón-Olvera R M, Núñez N O, González-Mancebo D, Monje-Moreno J M, Muñoz-Rui M J, Gómez-González E, Arroyo E, Torres-Herrero B, de la Fuente J M and Ocaña M 2023 Europium doped-double sodium bismuth molybdate nanoparticles as contrast agents for luminescence bioimaging and x-ray computed tomography *Inorg. Chem. Front.* **10** 3202–12
[14] Isik M, Altuntas G, Gasanly N M and Darvishov N H 2025 $NaBi(MoO_4)_2$ crystal: defect states and luminescence properties for optoelectronic applications *Mater. Lett.* **383** 137990
[15] Ren T, Xing P, Wang L, Cao Z, Cheng Z, Xiao Y, Wang F, Zhao E and Zhang S 2025 Remarkable flexo-photocatalytic organic pollutant degradation by oxygen vacancy engineered nonpolar $NaBi(MoO_4)_2$ nanospheres *Adv. Powder Technol.* **36** 105129
[16] Zhu C, Guo W, Du F, Fu P, Deng Q and Lin Z 2018 One-pot synthesis of $NaBi(MoO_4)_2$ nanorods and their gas-sensing properties *Mater. Lett.* **220** 172–74
[17] Turneaure S J and Gupta Y M 2022 Micro-strains, local stresses and coherently diffracting domain size in shock compressed Al(100) single crystals *J. Appl. Phys.* **131** 225902
[18] Lazar I, Szot K and Roleder K 2023 Influence of defects-induced stresses on birefringence in $SrTiO_3$ single crystals *Crystals* **13** 985
[19] Tian Y H, Liu F, Wang Y Y, Ramamurty U, Li B, Ren L B, Liu B Y and Shan Z W 2026 Bending-induced nanocrystallization enables large deformation in notched micron-sized single-crystal magnesium *Acta Mater.* 309 122062
[20] Shi X, He Z, Long S, Peng Y, Li D and Jiang S 2019 Loading rate effect on the mechanical behavior of brittle longmaxi shale in nanoindentation *Int. J. Hydrog. Energy* **44** 6481–90
[21] Borbély A 2022 The modified Williamson-Hall plot and dislocation density evaluation from diffraction peaks *Scr. Mater.* **217** 114768
[22] Gonzaga A C, Tavares S S M, Cardoso A S M, Dille J, Malet L and Pimenta A R 2025 Dislocation density measurements from x-ray diffraction of austenite and ferrite phases in superduplex UNS S39274 *J. Mater. Eng. Perform.* **34** 12525–36
[23] Althomali R H and Asif S U 2026 Unravelling the structure–magnetism coupling in al-substituted BaSrCa (1: 1: 2)-based ferrite nanoparticles *Mod. Phys. Lett. B* **40** 2650058
[24] Zou Y, Ge L F, Li Z Y, Guo J W, Zhu W and Ma Z S 2022 Determination of the intrinsic elastic modulus, hardness and fracture strength of thermally growth oxide by nanoindentation and tensile tests *Eng. Failure Anal.* **131** 105815
[25] Khan J A, Maithani Y, Horng R H and Singh J P 2022 Investigating mechanical properties of sintered $ZnGa_2O_4$ ceramics using nanoindentation *Ceram. Int.* **48** 27064–75
[26] Dadhich R, Korimilli E P and Singh I 2022 Microindentation response of relaxor ferroelectric PMN-0.32 PT single crystal *Ceram. Int.* **48** 29093–101
[27] Roubickova A, Tichy A, Vrbova R and Bradna P 2025 Indentation size effect in knoop and vickers hardness measurement of dental resin-based composites *J. Mech. Behav. Biomed. Mater.* **162** 106823
[28] Dadhich R and Singh I 2024 Effect of strain rate on the hardness of relaxor ferroelectric PMN-0.32 PT single crystals *Materialia* **33** 101983
[29] Petrík J, Blaško P, Markulík Š, Šolc M and Palfy P 2022 The indentation size effect (ISE) of metals *Crystals* **12** 795
[30] Yan C, Bor B, Plunkett A, Domènech B, Schneider G A and Giuntini D 2022 Nanoindentation of supercrystalline nanocomposites: linear relationship between elastic modulus and hardness: yan, bor, plunkett, domènech, schneider and giuntini *JOM* **74** 2261–76
[31] Zhang D and Li D Y 2023 A further look at the nano/micro-indentation method for measuring and ranking young's modulus and hardness of materials *Phys. Scr.* **98** 095936
[32] Benzarti Z, Khalfallah A, Evaristo M and Cavaleiro A 2022 Comparative study on the nanomechanical behavior and physical properties influenced by the epitaxial growth mechanisms of GaN thin films *Appl. Surf. Sci.* **579** 152188

[33] Ni Z, Chen Z, Chen G, Lu X, Chen G and Liu M 2025 Influence of the anisotropy of single crystal 4H-SiC on contact responses during nanoindentation and microscratch *Appl. Phys. A* **131** 206
[34] Yamamoto M, Tanaka M and Furukimi O 2021 Hardness–deformation energy relationship in metals and alloys: A comparative evaluation based on nanoindentation testing and thermodynamic consideration *Materials* **14** 7217
[35] Najafvandzadeh N, López-Moreno S, Errandonea D, Pavone P and Draxl C 2020 First-principles study of elastic and thermal properties of scheelite-type molybdates and tungstates *Mater. Today Commun.* **24** 101089
[36] Hanuza J, Haznar A, Maczka M, Pietraszko A, Lemiec A, Van der Maas J H and Lutz E T G 1997 Structure and vibrational properties of tetragonal scheelite $NaBi(MoO_4)_2$ *J. Raman Spectrosc.* **28** 953–63
[37] Wang X, Xiao Y, Tan W, Huang H, Yang D, Wang Y and Zhang B 2024 Computer-aided screening of bismuth molybdates nonlinear optical crystals γ-Bi_2MoO_6 *Inorg. Chem. Front.* **11** 7364–73